

Influence of the subtropical Andes on baroclinic disturbances: A Cold-front case study

Marcelo E. Seluchi

Centro de Previsão de Tempo e Estudos Climáticos (CPTEC)/INPE
São Paulo, Brazil

René D. Garreaud ()*

Department of Geophysics, Universidad de Chile, Santiago, Chile

Federico A. Norte

Programa Regional de Meteorología, Instituto Argentino de Nivología y Glaciología
(IANIGLA) CONICET. Mendoza, Argentina

A. Celeste Saulo

Centro de Investigaciones del Mar y la Atmósfera (CIMA)-CONICET
Departamento de Ciencias de la Atmósfera y los Océanos. Universidad de Buenos Aires,
Argentina

12 September 2005

(*) Corresponding author address
Dr. René Garreaud
P.O. Box 025285
Miami, FL 33102 – 5285. USA.
E-mail: rgarreau@dgf.uchile.cl

Abstract

The Andes Cordillera produces a significant disruption on the structure and evolution of the weather systems that cross South America. In particular, cold fronts tend to be “channeled” to the north immediately to the east of the Andes, fostering the advance of cold air incursions (cold surges) well into subtropical, and sometimes tropical, latitudes. In contrast, active cold fronts hardly reach subtropical latitudes along the western side of the Andes (Pacific sea border). Instead, as a cold front moves equatorward along the east side of the Andes, a marked low-level warming tends to appear along the west side of the subtropical Andes, leading to the formation of a mesoscale coastal low (or trough) in this region. In order to further understand the processes that lead contrasting evolution of the cold front at each side of the Andes, a typical frontal passage is studied in this work, using synoptic observations and a regional model (Eta/CPTEC) simulation.

The passage of the post-frontal anticyclone over southern South America produces a poleward pointing pressure gradient, and hence geostrophic easterly flow at low levels. The tall and steep mountains block the flow, leading to a very small zonal wind component close to the slopes. Convergence (divergence) of the zonal flow to the east (west) of the subtropical Andes is largely compensated by upward (downward) motion, and the associated cooling (warming) over this region. The weak zonal wind component near the Andes also breaks down the geostrophic balance over this region, giving rise to an acceleration of the southerly winds (i.e., along-barrier flow) and the consequent increase in cold advection. Therefore, to the east of the subtropical Andes both horizontal and vertical advection cool the lower troposphere, fostering the equatorward propagation of the cold front. To the west of the Andes, horizontal advection is largely offset by the strong warming associated to the enhanced subsidence over that region hindering the advance of the cold front into subtropical latitudes.

1. Introduction

The Andes cordillera is the largest and tallest mountain range in the Southern Hemisphere running continuously very close to the Pacific seaborder of South America. It impacts the atmospheric circulation in a broad range of scales, from the generation of mesoscale mountain waves (e.g., Seluchi *et al.* 2003) up to the positioning of planetary standing waves (e.g., Satyamurty *et al.* 1980). Between the southern tip of the continent and 38°S, the Andes elevation ranges between 1500-2500 m (Fig. 1) and then it rises sharply to about 5000 m ASL at subtropical latitudes (25-35°S). Thus, the subtropical Andes strongly block the zonal flow and separate two distinctive climatic regimes: a relatively cold a dry regime to the west, and a warmer and moister regime to the east (Seluchi and Marengo 2000).

At the synoptic scale, the Andes produce a marked disruption in the structure and evolution of the weather systems that cross the continent. Mid-latitude cyclones and anticyclones are “channeled” to the north immediately to the east of the Andes, fostering their extent into subtropical and tropical latitudes at the same time that their midlatitude cores move eastward (Gan and Rao 1994; Seluchi *et al.* 1998). Thus, cold fronts reach low latitudes several times per month. During wintertime, cold air incursions (sometime referred to as cold surges) might produce frost events as far north as southern Brazil and central Bolivia (e.g., Fortune and Kousky 1983, Hamilton and Tarifa 1977, Marengo *et al.* 1997, Garreaud 2000, Vera *et al.* 2002) with major social and economic impacts.

In contrast, frontal systems moving along the western side of the Andes (eastern Pacific) hardly reach subtropical latitudes with a noticeable effect (Ogaz and Fuenzalida 1981), partially explaining the extreme aridity of northern Chile and southern Peru. Furthermore,

as a warm ridge aloft approaches the continent, surface pressure to the west of the Andes tends to drop, leading to the formation of a coastal trough or low over central Chile (Garreaud *et al.* 2002; Garreaud and Rutllant 2003). Such coastal depressions are accompanied by warm and dry conditions near the coast and further inland, and strong low-level easterly flow down the Andean foothills (the so-called *Raco* winds; Rutllant and Garreaud 2004).

Synoptic experience indicates that cold air incursions to the east of the subtropical Andes and coastal depressions to the west tend to develop simultaneously, after the passage of a surface cold front over southern South America and in concert with the approach of a ridge aloft. Nevertheless, the dominant process behind the disruption of the synoptic-scale circulation is different across the mountain range, so as to produce opposite pressure tendencies and such a marked difference in the frontal displacement at each side of the subtropical Andes.

In order to further understand the processes that lead to the contrasting evolution of cold fronts at each side of the Andes, a typical frontal passage is studied in this work. The cold front was followed by a well-defined cold air incursion (to the east) and coastal low (to the west). To augment the observational data set used (described in section 2), the case was simulated numerically using the Eta/CPTEC model (detailed in section 3). The model results were validated and used to diagnose the episode in section 4. Our conclusions are presented in section 5.

2. Episode Overview

The selected case illustrates a typical frontal passage over southern South America, which took place from 13 to 18 of April 1999. In this section we present an overview of the episode using surface and upper air maps based on conventional synoptic reports.

On April 13 (Fig. 2a), a zonally oriented cold front reached the southern tip of South America while zonal wind prevailed over Patagonia (defined as the continental region south of 40°S). At subtropical latitudes the South Pacific anticyclone was slightly stronger than average and over the continent an incipient thermal-orographic low seated over northwestern Argentina near 27°S. During April 14 (Fig. 2b), the cold front moved equatorward reaching the northern Patagonia (40°S), in connection with a deepening surface low over the south Atlantic and a pronounced trough at mid-levels. To the north of the surface front, satellite imagery (not shown) reveals orographic clouds typical of Zonda wind aloft (Norte 1988, Seluchi *et al.* 2003). At the same time, the thermal-orographic low east of the Andes was deepening, accelerating northerly winds over north-central Argentina, Uruguay and southern Brazil.

On April 15, the active cold front reached northern Argentina favored by the cyclone development over the southwestern Atlantic. The stations in north-central Chile show little (if any) meridional thermal gradient or wind shift, so the front is hardly discernible to the west of the Andes. By 1200 UTC of this day (Fig. 2c) the cold-core, post-frontal anticyclone moved into the continent around 42°S. Note the cyclonic curvature of the isobars over the Andes, indicative of a restricted displacement of the anticyclone over this

region. The subsequent advance of the cold air overrode the thermal-orographic low east of the Andes. At mid and upper-levels the axis of the trough moved into the Atlantic seaborder, while the axis of the ridge was still off the Pacific coast. In between, strong southerly winds at 300 hPa over the Patagonia produce strong anticyclonic (positive) vorticity advection (Fig. 3).

During April 16 (Fig. 2d) the pressure begins to drop to the west of the subtropical Andes, leading to the formation of a coastal depression, an increase in air temperature, and the occurrence of low-level easterly flow. The subsidence warming also produces a clearing of the stratocumulus off central Chile (Fig. 4). Farther north along the western side of the Andes conditions remain mostly invariant. On the eastern side of the mountains, the active cold front has further advanced north of the tropic reaching central Bolivia and southern Brazil (around 15°S, see also Fig. 4) and freezing conditions were observed in central Argentina. The coastal low to the west and the intense anticyclone to the east produce an east-west surface pressure difference of almost 30 hPa across the subtropical Andes.

Finally, during April 17 the cold front tends to become stationary over southwestern Amazonia (not shown). In the next 24-48 hours the cold anticyclone (weakened at this time) moved eastward merging with the south Atlantic subtropical anticyclone (Dallavalle and Bosart 1975).

3. Model description and methodology

To obtain a synoptic and sub-synoptic description of the structural evolution of the cold front as it crossed the Andes, a numerical simulation of the episode was performed using

the Eta model version used in the Brazilian Center for Weather Forecasts and Climate Studies (CPTEC). The Eta/CPTEC is a regional model that uses the eta (η) vertical coordinate, defined by Mesinger (1984), in order to improve the calculation of horizontal magnitudes over sharp topography. The η -surfaces are practically horizontal even on mountain slopes, allowing a better representation of the horizontal variations of the atmospheric parameters in the presence of sharp topography (Mesinger and Black, 1992). The prognostic variables are temperature, specific humidity, winds, surface pressure, turbulent kinetic energy and cloud water. The equations are solved on the Arakawa-E grid and integrated through a split-explicit scheme based on forward-backward and Euler-backward schemes, both modified by Janjic (1979). The Eta/CPTEC regional model has been operationally used at CPTEC to provide weather forecasts over most of South America since late 1996.

The Eta/CPTEC was run with a 40 km horizontal grid spacing and 38 vertical layers with the model top placed at the 25 hPa level. The model includes a complete physics package with Betts and Miller (1986) scheme for convective precipitation modified by Janjic' (1994) and large scale precipitation solved in an explicit way (Zhao and Carr, 1997). Turbulent fluxes are represented through an updated Mellor and Yamada 2.5 order scheme. Surface heat and humidity fluxes are solved using the Monin-Obukov scheme, whereas the radiation package for both short wave and long wave radiation was developed at the Geophysical Fluid Dynamics Laboratory (GFDL) (Lacis and Hansen, 1974; Fels and Schwarzkopf, 1975). The soil scheme used in the current version of the Eta/CPTEC is the OSU (Oregon State University, Chen *et al.* 1996) model that includes three sub-superficial

layers and other in which vegetation canopy is simulated. For more details on model physics, see Black (1994).

Initial and boundary conditions were provided by the NCEP (National Centers for Environmental Prediction) operational analyses every six-hour for this simulation experiment. Annual climatology of soil moisture, seasonal fields of albedo and observed weekly mean sea surface temperatures are used as initial lower boundary conditions. The model domain and numerical settings are the same as those implemented in the operational version (Seluchi and Chou, 2001). The simulation length was set as 96 hours, extending from 0000 UTC April 14 through 0000 UTC April 18. Simulated fields were saved every three hours.

To facilitate the analysis of the physical processes that play in the frontal propagation, the simulation was divided in two periods. The “active” period was defined from the beginning of the simulation (0000 UTC, April 14) to the moment when the front became stationary at subtropical latitudes, approximately at 0000 UTC, April 17. The “demise” period extends from 0000 UTC, April 17, to the end of the simulation (0000 UTC, April 18).

Of particular interest for our analysis is the thermodynamic equation, which in η vertical coordinate is written as:

$$\frac{\partial T}{\partial t} = -\vec{V} \bullet \nabla_{\eta} T - \dot{\eta} \frac{\partial T}{\partial \eta} + \frac{\chi T \omega}{p} + \frac{\dot{Q}}{C_p} \quad (1)$$

where T is temperature, \vec{V} is the horizontal wind vector, ω is vertical velocity in pressure coordinates, χ is $R(c_p)^{-1}$; $\dot{\eta}$ is the vertical velocity in η -coordinates and \dot{Q}/C_p represents diabatic sources/sinks.

Proper treatment of each individual term, allowed a quantitative assessment of the relative contribution of each process relevant in the simulated temperature changes. The second and third terms in the r.h.s. of (1) will be handled together, since they are due to adiabatic ascents and or descents, and will be referred to as the “static stability” term (e.g. Bluestein, 1993). The diabatic source/sink term will be splitted into three main contributions: (a) “moisture processes”, which includes warming/cooling due to large scale condensation and cumulus convection, (b) “radiation” that takes into account the temperature changes associated to radiative transfers in the atmosphere, and (c) “surface processes”, derived from surface fluxes. This selection of terms was preferred since some processes involved are essentially similar and/or because a detailed examination of their differences is beyond the scope of this paper (e.g., the relative contribution of large scale condensation versus that coming from cumulus convection). Also, when the relative contribution of a process is not significant, as happens with diffusive terms, it will not be included in the discussion. Accordingly, the thermodynamic equation is schematically represented as the sum of horizontal advection, static stability, moisture processes, radiation and surface processes. Each one of these terms has been archived directly form the model code for each time-step (96 seg) in order to minimize computational residuals.

4. Results

4.1 Temporal evolution and spatial structure

Figure 5 shows the evolution of the surface pressure in nine stations located at both sides of the Andes (see Fig. 1). At midlatitudes (Fig. 5a) the pressure follows a similar trend at both sides, characterized by a sustained increase from the passage of the surface low up to a maximum nearly simultaneous during April 16 associated with the center of the post-frontal anticyclone. In contrast, significant differences across the mountain are found at subtropical latitudes (Fig. 5b). A weak maximum in Quintero (west side) occurs at the beginning of the 15, very early within the simulation period, followed by a gentle decrease that indicates the development of the coastal low in central Chile. At the other side of the mountains the pressure experiences a marked increase during April 15 and 16, particularly in Mendoza, the station closest to the Andes. At tropical latitudes (Fig. 5c) the surface pressure at the west side (Antofagasta) remains nearly invariant during this period, while the surface pressure near the eastern slope of the Andes (Las Lomitas) exhibits a pronounced increase during April 16 remaining high during most of the 17th. In Londrina, located farther east, the pressure increases less than and at a later time than at Las Lomitas.

For comparison, Fig. 6 includes the simulated time series of the surface pressure at the grid points closest to the stations used in Fig. 5. To the east of the Andes the model tends to over-estimate the maximum in surface pressure associated with the post-frontal anticyclone, while to the west of the subtropical Andes (33°S) the simulated minimum associated with the coastal low is weaker and occurs earlier than its observational counterpart at Quintero. Despite these problems, the model was able to capture quite well

the differential evolution of the surface pressure at tropical and subtropical latitudes, and the more similar evolution in midlatitudes, lending support to the use of model outputs to further describe and diagnose this event. Moreover, the simulated spatial structure of the surface pressure field near the time of maximum pressure gradient across the subtropical Andes agrees well with the manual analysis (c.f. Fig. 7 and Fig. 2d), but for a weaker coastal low and more equatorward positioning of the cold core anticyclone.

The trace of the cold front using maps of model-derived low-level air temperature is qualitative similar to the hand-made analysis shown in Fig. 2. The most striking feature is the differential advance of the front at each side of the Andes, illustrated in Fig. 8 by a time-latitude cross section of the 850 hPa air temperature along 75°W (over the Pacific Ocean) and 60°W (over the continent, to the east of the Andes). Over the continent (Fig. 8b), the cold air advances equatorward continuously at about 10 m/s from 14 April until 17 April, when the cold front becomes stationary at 15°S. There is frontogenesis during most of this period, as the front encounters increasingly warm air. Cross sections at other levels (not shown) reveal that the depth of the cold air dome is about 3 km, decreasing only slightly as it moves into lower latitudes.

The cold air at 850 hPa to the west of the Andes (Fig. 8a) moves equatorward until 1200 UTC April 15, and much slower than its counterpart to the east, so the cold front at this level reaches only to 34°S. Baroclinicity is small, because of the cool air temperatures that prevail over the Pacific Ocean prior to the cold front arrival. By the end of April 15 a warming begins at subtropical latitudes that later on expands southward, increasing the north-south temperature contrast. Close to the surface the cold air advances for a longer

time and further north than aloft; for instance, at 950 hPa the cold front did arrive at 30°S on 0000 UTC April 16 (not shown).

Figure 9 shows the change of temperature and geopotential during the active period in a longitude-pressure cross section at 33°S and 23°S. At 33°S (Fig. 9b), low level (1000-700 hPa) air temperature increased about 10°C to the west of the Andes and decreased a similar amount to the east, building up a strong low-level zonal temperature gradient (albeit interrupted by the Andes). Thus, by the end of this period, 850 hPa air temperatures exceeded 15°C to the west of the Andes, while remained below 5°C to the east. At 23°S (Fig. 9a) the low-level cooling and ridging to the east of the Andes have similar values than those observed at 33°S, but over a narrower region near foothills. To the west of mountains, warming and geopotential decrease are still observed but with almost neglectible magnitudes. Consistent with the weather maps (Fig. 2), these changes in air temperature clearly indicate that the cold front did arrive to subtropical latitudes (and moved father north) to the east of the Andes, but it failed to do so along the west coast of the continent.

4.2 Model Diagnosis

The thermodynamics analysis is key to determine the leading processes that control the evolution of the cold front. Furthermore, as suggested by Fig. 9 and confirmed by the hypsometric equation, surface pressure changes are mostly hydrostatically driven by low-level (1000-700 hPa) air temperature changes over most of the domain. Fig. 10 shows the 700-1000 hPa temperature tendencies associated with each of the terms of the thermodynamic equation (see section 3) during the active period.

A zonal band of cold advection is found over the continent between 33°-42°S (Fig. 10a), with similar values at each side of the Andes, in connection with southerly winds behind the cold front. A northward extension of the area of cold advection (to the north of 30°S) is found immediately to the east of the Andes presumably associated with easterly winds that flow toward the warm-core Northwestern Argentinean Low (Seluchi *et al.* 2003).

In contrast with the horizontal advection term, the static stability (vertical) term exhibit a pronounced difference across the mountains (Fig. 10b). To the north of 30°S ascending motion leads to negative temperature tendencies along the surface front (Paraguay, southern Brazil and the southeast Atlantic) and along the eastern slope of the subtropical Andes, while smaller but positive tendencies prevail along the western slope. To the south of 30°S, synoptic-scale subsidence over the post-frontal anticyclone produces positive temperature tendencies over the continent and the adjacent Pacific Ocean. To the west of the Andes, however, the low-level warming is about three times larger than to the east.

Latent heat release over the frontal region leads to positive temperature tendencies (Fig. 10c) over the Atlantic off the Uruguay and Argentina coast, as well as over the eastern side of the subtropical Andes where cloud formation is instigated by the upslope flow. The positive contribution of the moist processes is, however, mostly compensated by the adiabatic cooling in the regions of ascending motion (c.f. Fig. 10b and 10c). Radiative processes lead to a uniform cooling of the 700-1000 hPa layer (Fig. 10d), partially compensated by the surface warming (Fig. 10e).

Finally, Fig. 10f shows the sum of the temperature tendencies by each of the analyzed processes. This field results very close to the actual temperature tendency (modeled local rate of change, not shown) lending support to the employed methodology. Positive (negative) tendencies are found to the west (east) of the Andes. Such marked cross-mountain difference is largely due to the strong and differential effect of the static-stability term across the Andes superimposed on the rest of the effects that are nearly uniform across the Andes (horizontal advection) or have small amplitude (diabatic terms).

To further describe the mechanisms responsible for the temperature changes and the frontal displacement, Fig. 11 includes the leading terms of the thermodynamic equation expressed as the temporal evolution of the accumulated tendencies for 6 boxes across the domain (three at each side of the Andes). The total tendency in the two southernmost boxes (37° - 42° S) exhibits a qualitatively similar behavior, with a cooling from the beginning of the simulation and a subsequent warming. Because of the difference in longitude, the transition from cooling to warming occurs about 20 hr later to the east of the Andes with respect to the west. In both boxes, the warming is due to vertical advection not compensated by cold horizontal advection.

At subtropical latitudes (30° - 35° S) and to the west of the Andes, warming prevails during the whole period, especially after 1200 UTC April 15, driven by strong vertical warming (subsidence) that is nearly twice as large as the horizontal cold advection. The vertical warming begins before the southerly cold advection, thus preventing the passage of the cold front further north. To the east of the Andes, horizontal cold advection has a similar value than to the west, but vertical advection is now negative, leading to a cooling tendency

during most of the period. The tendency due to moist processes is very small, indicative that the cold front was devoid of significant low and middle clouds when it crosses this range of latitudes.

In the northernmost boxes (20° - 25° S), the temperature tendencies also differ markedly across the Andes. To the west, the total tendency is neglectable, with a nearly perfect balance between vertical warming and radiative cooling (as expected for a region covered by marine stratocumulus). Horizontal advection remains near zero, consistent with the no arrival of the front to these latitudes. To the east, the significant cooling begins at 0000 UTC April 16, forced by both horizontal and vertical advection. The vertical advection is, however, mostly compensated by the latent heat release in the cloudiness ahead and at the cold front, as corroborated by the satellite imagery shown in Fig. 4.

What causes the larger static-stability warming to the west of the Andes with respect to the east side? The answer resides on the magnitude of the vertical velocity, as shown in Fig. 12 by a longitude-height section along 33° S and 23° S of the vertical (ω) wind. Subsidence (and hence warming) is found to the west of the Andes, specially strong at 33° S, with a maximum between 900-700 hPa very close to the mountain slope. Large-scale subsidence at mid levels is interrupted over the continent to the east of the subtropical Andes and reappears over the Atlantic. Ascending motion has a maximum very close to the eastern Andean slope at 23° S, but is also present at 33° S.

Figure 12 also shows the zonal wind component. Westerly flow prevails at upper- and mid-levels, with some evidence of gravity wave activity above and downwind of the Andean ridge level at 33° S where the westerlies are stronger than at 23° S. In contrast, easterly flow

dominates below 800 hPa over the continent and the adjacent Pacific Ocean, driven by the post-frontal anticyclone. The easterlies, however, exhibit a pronounced change in magnitude due to the upwind (east) and downwind (west) barrier effects of the Andes cordillera. To the east of the Andes the easterly flow is largely blocked by the high and very steep terrain (the Froude number results much less than 1), so the zonal component of the wind becomes very small near the foothills. This condition leads to the breakdown of the geostrophic balance, accelerating the southerly winds over central Argentina. A more detailed analysis of this process is presented in Garreaud (2001).

Similarly, the steep western slope of the Andes restricts the low-level zonal flow in this region. For instance, in the zonal cross-section in Fig. 12b (33°S) the easterlies at 900 hPa are near zero immediately to the west of the Andes but increase up to 6 m/s within 500 km off the coast. The mass continuity equation evaluated using the model outputs on a grid box at 850 hPa and 150 km west of the Andes slope reveals that such strong divergence in zonal flow is largely compensated by enhanced subsidence, since the meridional wind component, although stronger than the zonal component ($v \sim 10 \text{ ms}^{-1}$), varies little along the coast. The topographically enhanced subsidence takes place in a very stable environment, and hence, it leads to strong warming of the lower and middle troposphere west of the subtropical Andes. In a study of a coastal low in central Chile, Garreaud and Rutllant (2003) also showed that low-level vertical warming leads to coastal troughing, and that intensified alongshore cold advection during this event was nearly offset by the offshore warm advection.

A thermodynamic analysis for the demise period (from 0000 UTC April 17 to 0000 UTC April 18) is shown in Fig. 13. During this stage, the cold front over the continent moved as far north as 15°S, as evidenced by the negative tendencies due to horizontal advection (Fig. 13a). Nevertheless, over the Bolivian lowlands and western Brazil the warming due to subsidence (Fig. 13b), radiative balance (Fig. 13c) and moist processes (not shown) offset the horizontal cold advection, hence the total temperature tendency (Fig. 13d) is slightly positive, indicating frontolysis. Farther south and over the subtropical Atlantic ocean, cold advection still prevails but is largely compensated by the postfrontal subsidence. To the west of the Andes and over the subtropical Pacific ocean, slightly negative radiative cooling is nearly balanced by subsidence warming.

5. Conclusions

The Eta-CPTEC model was used to simulate and diagnose the passage of a cold front over southern South America, whose structural evolution is markedly influenced by the Andes cordillera at subtropical latitudes. The event took place in mid-April 1999, and was selected because exhibits typical features of frontal passages in this region. In particular, as the parent depression moved into the south Atlantic and a mid-level ridge approached the western coast of the continent, the northward edge of the low-level front and the postfrontal anticyclone experienced a quite contrasting evolution at each side of the mountains.

To the east side of the Andes, a dome of cold air between the surface and about 700 hPa advanced well into subtropical latitudes at about 10 m/s, so the cold front could be traced up to about 15°S. Associated with the post-frontal anticyclone, freezing conditions were observed in the morning of April 16 over central Argentina. In sharp contrast, the dome of

cold air becomes very shallow as advance over the eastern Pacific bounded by the western slope of the Andes. Even near the surface, the cold air reaches only up to 30°S. At subtropical latitudes the low-level air temperature actually increased by more than 10°C with respect to the “pre-frontal” conditions, leading to the formation of a coastal low over central Chile nearly at the same time of the passage of the cold surge over central Argentina. Farther north along this coast, conditions remain almost invariable.

In order to synthesize our analysis, Fig. 14 shows maps of air temperature, winds and vertical velocity at 850 hPa at four instants during the simulation. Early in the simulation (1200 UTC April 14, Fig. 14a) the cold front can be identified at both sides of the Andes at about 35°S, with southerly cold advection behind it. Over the continent, strong ascent is found over the front while subsidence prevails farther south in connection with the post-frontal anticyclone; over the Pacific, there is only an interruption of the subsidence associated with the subtropical and the post-frontal anticyclones. A meridional band of ascending motion is found to the south of 35°S as the westerly flow surpasses the Andes cordillera. Twelve hours later (Fig. 14b) cold advection is present at both sides of the Andes, but low-level wind develops a subtle *easterly* component at subtropical latitudes in response to the anticyclone farther south. The tall and steep mountains effectively block the flow, leading to a very small zonal wind component close to the slopes. Convergence (divergence) of the zonal flow to the east (west) of the subtropical Andes is largely compensated by upward (downward) motion, and the associated cooling (warming) over this region.

At 1200 UTC April 15 (Fig. 14c), the easterly flow is very clear at both sides of the Andes. To the west side of the mountains, the subsidence warming offset the horizontal cold advection, limiting the advance of the cold front in this region. Moreover, horizontal cold advection has decreased since winds become almost parallel to the isotherms off the coast. In contrast, to the east of the Andes the vertical advection acts in concert with the horizontal advection. The blocking effect of the Andes also breaks down the geostrophic balance, accelerating the southerly winds over the continent and fostering the rapid advance of the cold front over the continent. By 1200 UTC April 16 (Fig. 14d), the cold air reached Bolivia and southwest Brazil helped by horizontal and vertical advection. Later on, however, warming due to postfrontal subsidence, radiation and moist processes lead the temperature tendency, beginning the frontolysis. To the west of the Andes the coastal area of warm air reaches its maximum extent (25°S-36°S), follow by a progressive shrinking as subsidence begins to decrease, in connection with an incoming mid-level trough.

In summary, the differential evolution of the cold air dome at each side of the Andes is due to the blocking effect of the cordillera upon the low-level flow. The decrease of the easterlies near the eastern foothills leads to ascending motion and vertical cooling, as well as an acceleration of the southerly) winds that advects cold air, contributing to the advance of the cold front. The increase of the easterlies off the coast is compensated by subsidence to the west of the Andes, hindering the frontal advance in this region.

Acknowledgments

This work was partially funded by the Ministry of Science and Technology of Brazil through the Projects AC-61 and 490353/2004-5 of the PROSUL Program.

References

Betts A. K., and Miller M. J., 1986: A new convective adjustment scheme. Part II: Single column test using GATE wave, BOMEX, and arctic air-masses data sets. *Quart. J. Roy. Meteorol. Soc.*, **112**, 1306-1335.

Black T. L., 1994: The new NMC mesoscale Eta model: Description and forecast examples. *Wea. Forecasting*, **9**, 256-278.

Bluestein H. B., 1993: *Synoptic-dynamic meteorology in midlatitudes, Volume II: Observations and theory of weather systems*. Oxford University Press, 953 pp.

Chen F., and co-authors, 1996: Modeling of land surface evaporation by four schemes and comparison with FIFE observations, *J. Geoph. Res.*, **101**, D3,7251-7268.

Dallavalle J.P., and Bosart L.F., 1975: A synoptic investigation of anticyclogenesis accompanying North American polar air outbreaks. *Mon. Wea. Rev.*, **131**, 891-908,

Fortune M.A., and Kousky V.E. 1983: Two severe freezes in Brasil: precursors and synoptic evolution. *Mon. Wea. Rev.*, **111**, 181-196.

Fels, S. B., and M. D. Schwarzkopf, 1975: The simplified exchange approximation: A new method for radiative transfer calculations. *J. Atmos. Sci.*, **32**, 1475-1488.

Gan, M.A.; and Rao V.B., 1994: The influence of the Andes Cordillera on Transient disturbances. *Mon. Wea. Rev.* **122**, 1141-1157.

Garreaud, R.D. and J. Rutllant, 2003: Coastal lows along the subtropical west coast of South America: Numerical simulation of a typical caso. *Mon. Wea. Rev.*, **131**, 891-908.

Garreaud, R.D., J. Rutllant, and H. Fuenzalida, 2002: Coastal lows along the subtropical west coast of South America: Mean structure and evolution. *Mon. Wea. Rev.*, **130**, 75-88.

Garreaud, R.D., 1999: Cold air incursions over subtropical and tropical South America. A numerical case study. *Mon. Wea. Rev.*, **127**, 2823-2853.

Garreaud, R. D., 2000b: Cold air incursions over Subtropical South America: Mean structure and dynamics. *Mon. Wea. Rev.*, **128**, 2544-2559.

Gill, A.E., 1982: *Atmosphere-Ocean Dynamics*. International Geophysics Series. Vol. 30. Academic Press. 662 Pp.

Hamilton, G. M., and Tarifa R.J.,1978: Synoptic aspects of a polar outbreak leading to frost in tropical Brazil, July 1972. *Mon. Wea. Rev.*, **106**, 1545-1556.

Janjic' Z. I., 1994: The step-mountain eta coordinate model: further developments of the convection viscous sublayer and turbulence closure schemes. *Mon. Wea. Rev.*, **122**, 927-945.

Janjic'. Z. I., 1979: Forward-backward scheme modified to prevent two-grid-interval noise and its application in sigma coordinate models. *Contrib. Atmos. Phys*, **52**,69-84.

Lacis, A. A., and J. E. Hansen, 1974: A parameterization of the absorption of solar radiation in the earth's atmosphere. *J. Atmos. Sci.*, **31**, 118-133.

Marengo, J., A. Cornejo, P. Satyamurty, C. Nobre and W. Sea, 1997: Cold surges in tropical and extratropical South America: The strong event en June 1994. *Mon. Wea. Rev.*, **125**, 2759-2786.

Mesinger F., and Black T.L., 1992: On the impact on forecast accuracy of the step-mountain (eta) vs. sigma coordinate. *Meteor. Atmos. Phys*, **50**, 47-60.

Mesinger F., 1984: A blocking technique for representation of mountains in atmospheric models. *Riv. Meteorol. Aeronaut.*, **44**, 195-202.

Norte F. A., 1988: Características del viento Zonda en la Región de Cuyo. PhD Thesis. Available at Programa Regional del Meteorología, CRICYT, Mendoza, and *Departamento de Ciencias de la Atmosfera, Ciudad Universitaria (1428) Buenos Aires, Argentina*].

Ogaz, P., and H. Fuenzalida 1981: Acerca de un paso frontal y sus manifestaciones en el litoral árido del norte de Chile. *Tralka*, **2**, 19-38.

Rutllant, J. and R.D. Garreaud, 1995: Meteorological air pollution potential for Santiago, Chile: Towards an objective episode forecasting. *Environmental Monitoring and Assessment*, **34**(3), 223-244.

Rutllant J. and R. Garreaud, 2004: Episodes of strong flow down the western slope of the subtropical Andes. *Mon. Wea. Rev.*, **132**, 611-622.

Satyamurty P., Pinheiro Dos Santos R., and Maringolo Lemes M.A., 1980: On the stationary trough generated by the Andes. *Mon. Wea. Rev.*, **108** , 510-520.

Seluchi M. E., A. C Saulo, M Nicolini and P Satyamurty, 2003: The Northwestern Argentinean Low: a study of two typical events. *Mon Wea Rev*, **131**, 2361-2378.

Seluchi, M.E., Norte F.A., Satyamurty P., and Chou S.C, 2003: Analysis of three situations of Foehn effect over the Andes (Zonda wind) using the Eta/CPTEC regional model. *Wea & Forec*, **18**, 481-501.

Seluchi, M. E., and S.Ch Chou, 2001: Evaluation of two Eta Model versions for weather forecast over South America, *Geofís. Int.*, **40**, 219-237

Seluchi, M.E., and Margengo J.A., 2000: Tropical-extratropical exchange of air masses during Summer and Winter in South America: climatic aspects and extreme. *Int. J. Climat.*, **20**, 1167-1190.

Seluchi, M.E., H. Le Treut and V.Y. Serafini, 1998: The impact of the Andes cordillera on the transient activity: A comparison between observations and the LMD-GCM. *Mon. Wea. Rev.*, **126**, 18 pp.

Vera, C. S., P.Vigliarolo and H.E. Berbery, 2002: Cold sesason synoptic waves over subtropical South América. *Mon. Wea. Rev.*, **130**, 684-699.

Zhao, Q., and F. H. Carr, 1997: A prognostic cloud scheme for operational NWP Models. *Mon.Wea. Rev.*, **125**, 1931-1953.

Figure Captions

Figure 1. Topographic map of southern South America (elevations higher than 500 m are shaded) and location of the meteorological stations.

Figure 2. Surface analysis corresponding to (a) 1200 UTC 13 April 1999, (b) 1200 UTC 14 April 1999, (c) 1200 UTC 15 April 1999 and (d) 1200 UTC 16 April 1999. Isobars (solid lines) are drawn at 5 hPa intervals (only the two last numbers are plotted) and wind barbs are in knots ($1 \text{ knot} \approx 0.5 \text{ ms}^{-1}$).

Figure 3. NCEP-NCAR reanalyzed geopotential height (solid lines, contoured every 90 m) and wind velocity (m/s; values higher than 25 m/s are shaded) at the 300 hPa level corresponding to 1200 UTC 16 August 1999.

Figure 4. GOES-8 infrared (Channel IV) satellite image corresponding to 1200 UTC 16 April 1999.

Figure 5. Time evolution of sea level pressure (hPa) observed at (a) P. Montt (dashed line), Neuquen (dashed) and Viedma (solid), (b) Quintero (dotted), Mendoza (solid) and Junin (dashed) and (c) Antofagasta (dotted), Las Lomitas (solid) and Londrina (dashed). The band of longitude in which the stations are located is indicated at the top of each panel. See also Fig. 1 for station location.

Figure 6. Time evolution of the simulated sea level pressure (hPa) for the grid points closest to the stations used in Fig. 5 and using the same bands of latitude.

Figure 7. Sea level pressure (solid lines, contoured every 3 hPa) and 500/1000 hPa thickness (dashed line, contoured every 60 gpm) as simulated by the Eta/CPTEC Model valid for 1200 UTC 16 April 1999 (60 hr simulation).

Figure 8. Latitude-time cross section of the 850 hPa air temperature (contoured every 3°C), negative values in dashed lines) along a) 75°W and b) 65°W. Light (dark) shaded indicates temperature gradient in excess of 3°C/100 km (6°C/100 km).

Figure 9. Vertical cross section at a) 23°S and b) 33°S of geopotential height change (contoured every 40 gpm) and temperature tendency (°C, shades) for the during the 0000 UTC April 14 to 0000 UTC April 17 (a) and 00000 UTC April 16 to 00000 UTC April 17 (b) periods. Model topographic profile is included.

Figure 10. Temperature tendency (°C) averaged between surface and 700 hPa levels associated with each of the terms of the thermodynamic equation in η coordinates (Eta/CPTEC simulation) during the active period (from 0000 UTC April 14 through 0000 UTC April 17). Boxes indicated in panel d) were used to perform the temporal evolution showed in Figure 11.

Figure 11. Temporal evolution of the temperature tendency (°C) averaged between surface and 700 hPa levels associated with each of the terms of the thermodynamic equation in η coordinates (Eta/CPTEC simulation) averaged over the indicated boxes (illustrated in panel d) of Figure 10).

Figure 12. Vertical cross section at a) 23°S and b) 33°S of the vertical omega (hPa/s, shaded) and zonal wind (contours, m/s) averaged between a) 0000 UTC April 14 and 0000 UTC April 17 and b) 0000 16 UTC April 16 and 0000 UTC April 17 from Eta/CPTEC simulations. Model topographic profile is included.

Figure 13. As Fig. 10 but for the decaying period (from 0000 UTC April 17 through 0000 UTC April 18). Panels correspond to the partial contribution of (a) horizontal advection, (b) static stability, (c) Radiation + surface processes, and (d) the sum of all the partial contributions (including those derived from moisture processes).

Figure 14. Temperature contours (contoured every 3°C), wind vectors (m/s) and omega vertical velocity (hPa/s) at the 850 hPa level, corresponding to 1200 UTC April 14 (upper left panel), 1000 UTC April 15 (upper right panel), 1200 UTC April 15 (lower left panel) and 1200 UTC April 16 (lower right panel).

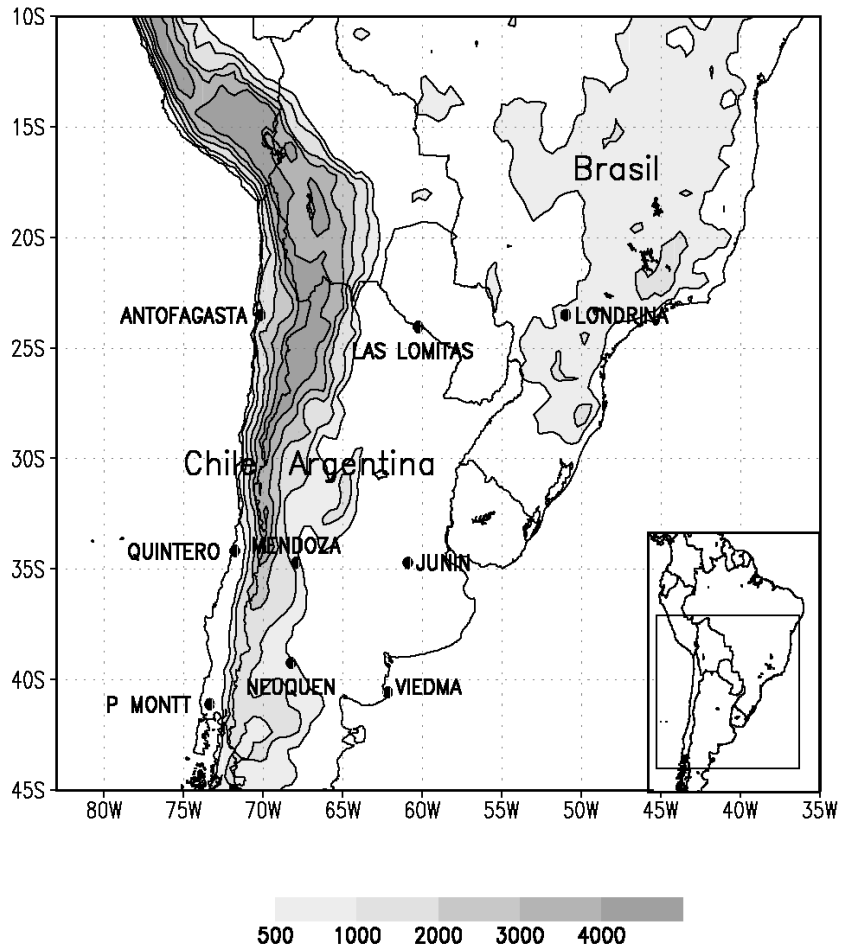


Figure 1. Map of the region under study, including topography (elevations higher than 500 m are shaded) and location of the meteorological stations.

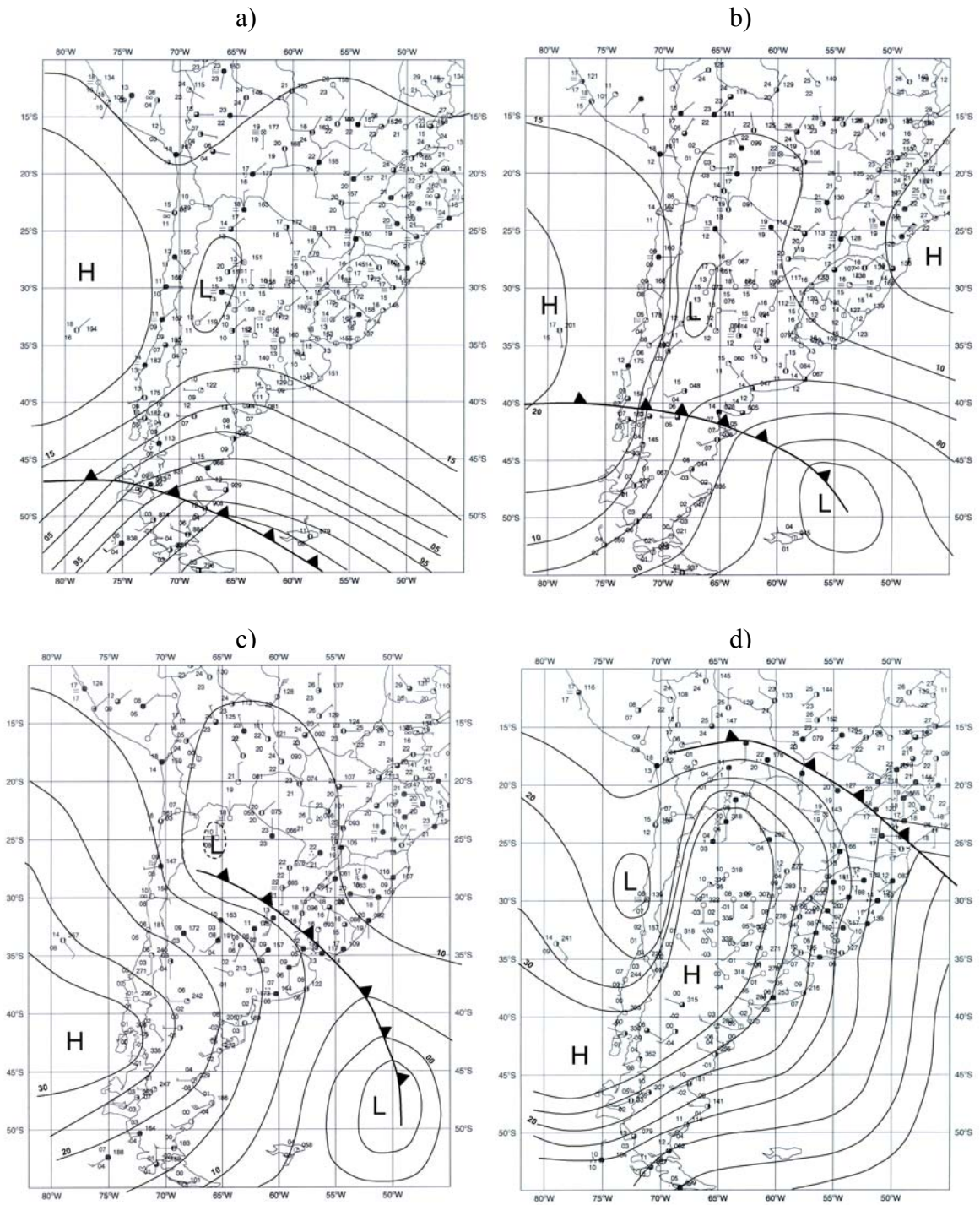


Figure 2. Surface analysis corresponding to (a) 1200 UTC 13 April 1999, (b) 1200 UTC 14 April 1999, (c) 1200 UTC 15 April 1999 and (d) 1200 UTC 16 April 1999. Isobars (solid lines) are drawn at 5 hPa intervals (only the two last numbers are plotted) and wind barbs are in knots ($1 \text{ knot} \approx 0.5 \text{ ms}^{-1}$).

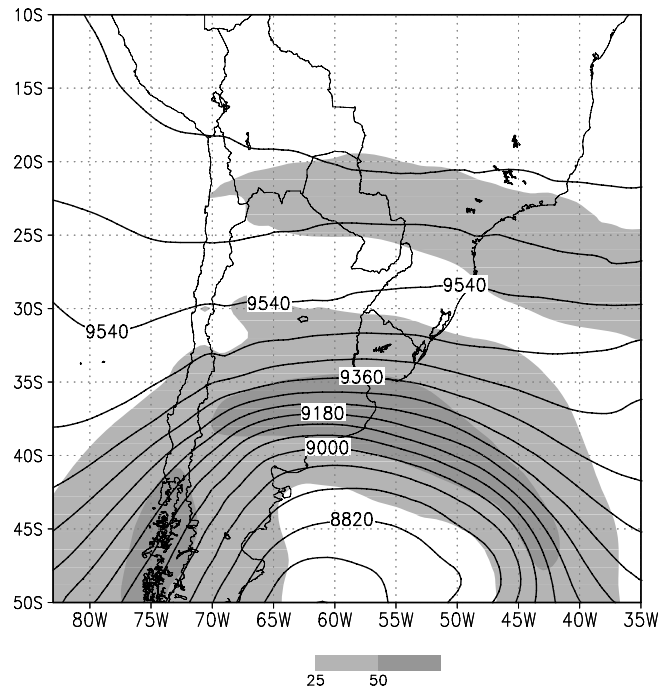


Figure 3. Geopotential height (solid lines, contoured every 90 m) and wind velocity (m/s; values higher than 25 m/s are shaded) at the 300 hPa level corresponding to 12:00 UTC 16 August 1999.

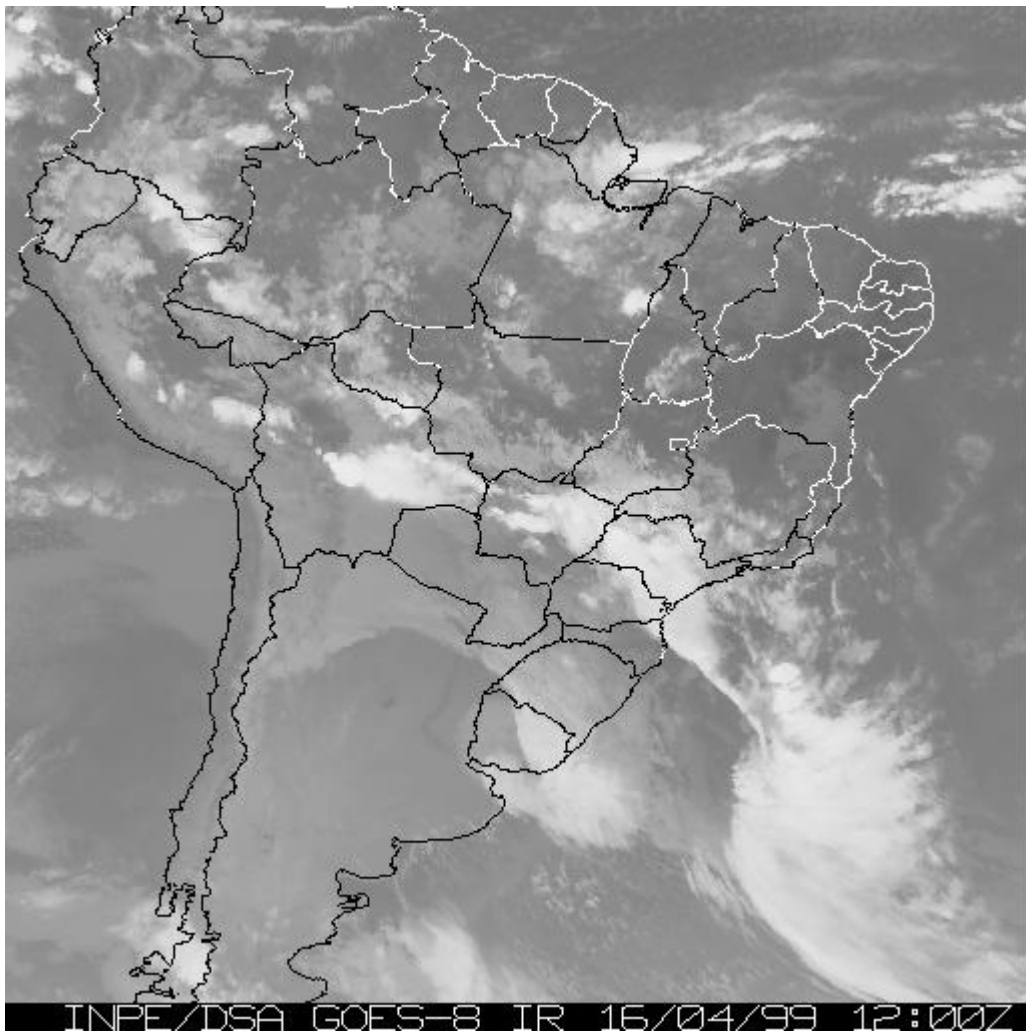


Figure 4. GOES-8 infrared (Channel IV) satellite image corresponding to 1200 UTC 16 April 1999

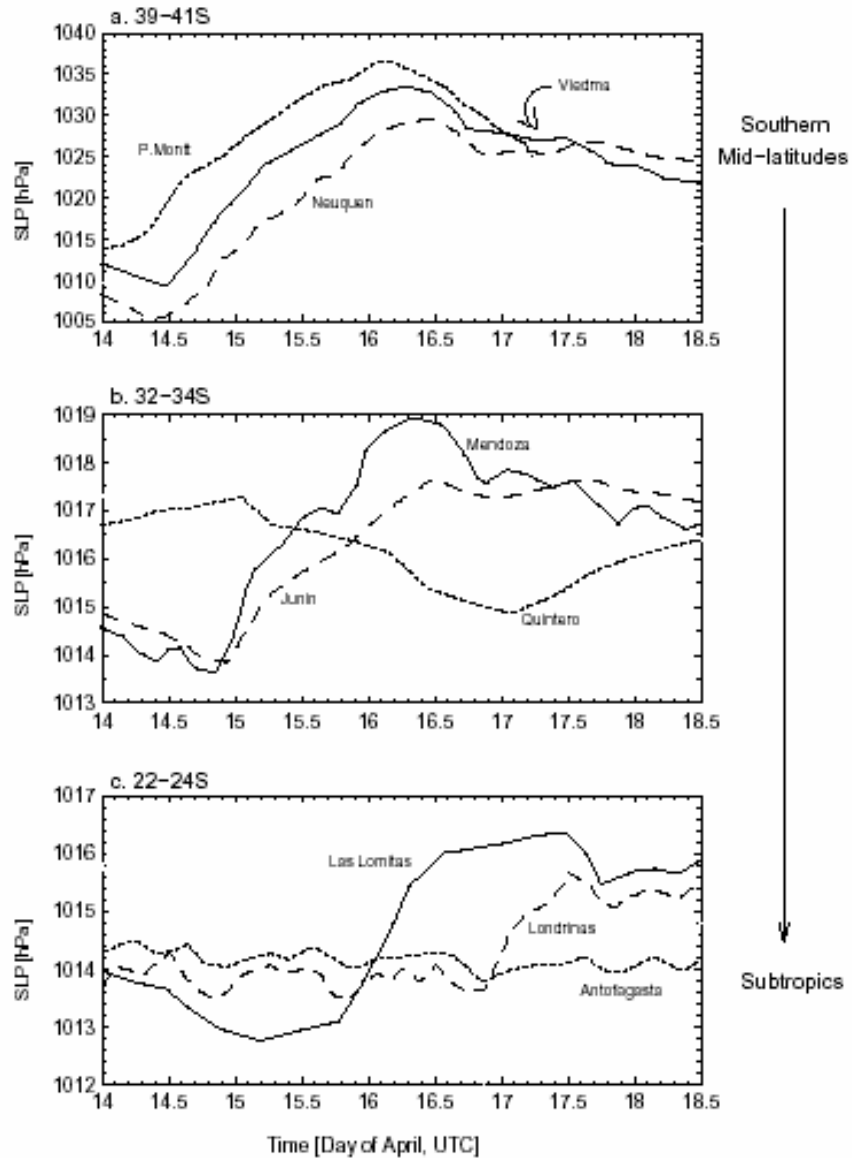


Figure 5. Temporal evolution of sea level pressure (hPa) observed at (a) P. Montt (dashed line), Neuquen (dashed) and Viedma (solid), (b) Quintero (dotted), Mendoza (solid) and Junin (dashed) and (c) Antofagasta (dotted), Las Lomitas (solid) and Londrina (dashed). The band of longitude in which the stations are located is indicated at the top of each panel. See also Fig. 1 for station location.

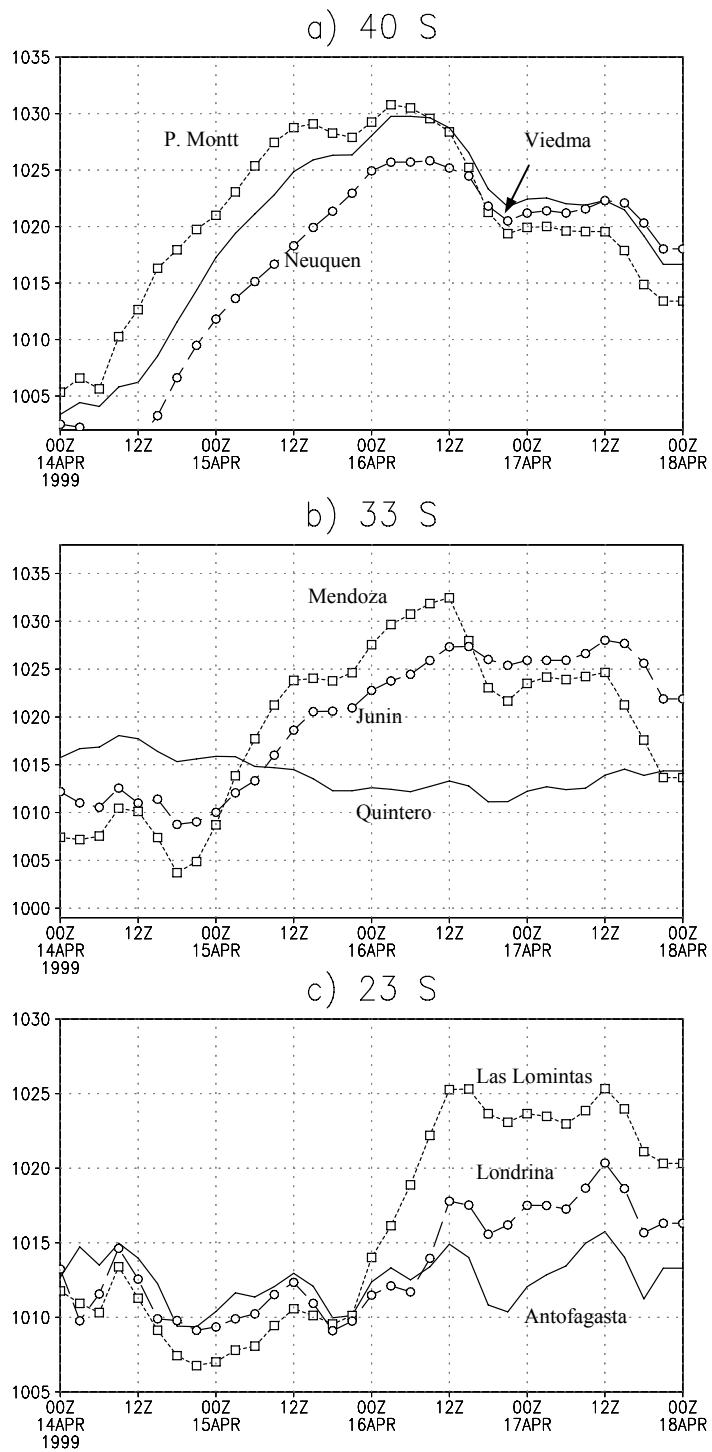


Figure 6. As in Fig. 5 but obtained from Eta/CPTEC model simulations. In this case, we display the simulated time series of the surface pressure at the grid points closest to the stations used in Fig. 5.

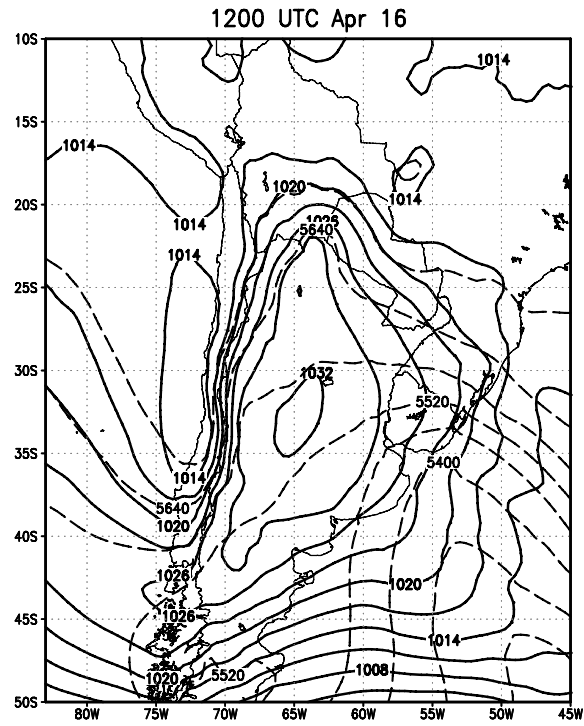


Figure 7. Sea level pressure (solid lines, contoured every 3 hPa) and 500/1000 hPa thickness (dashed line, contoured every 60 gpm) as simulated by the Eta/CPTEC Model valid for 1200 UTC 16 April 1999 (60 hs simulation).

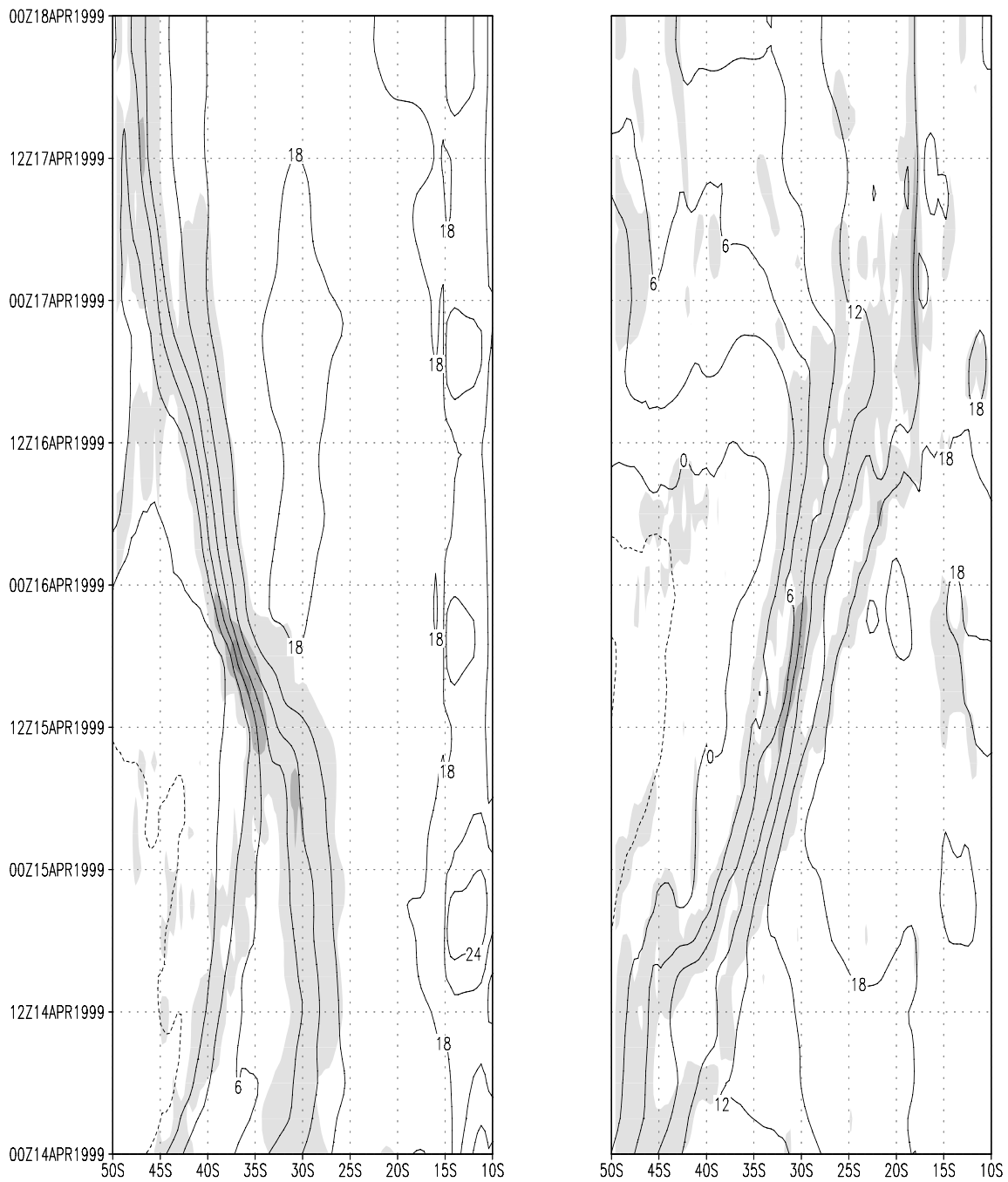
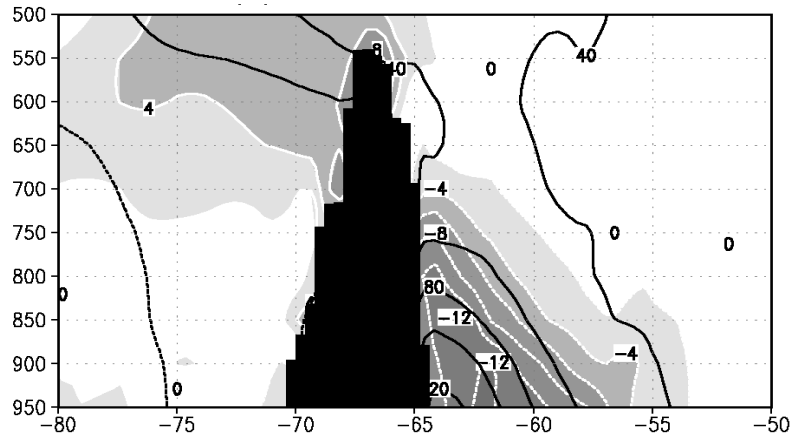


Figure 8: Latitude-time cross section of the 850 hPa air temperature (contoured every 3°C|, negative values in dashed lines) along a) 75°W and b) 65°W. Light (dark) shaded indicates temperature gradient in excess of 3°C/100 km (6°C/100 km).

a) 23°S



b) 33°S

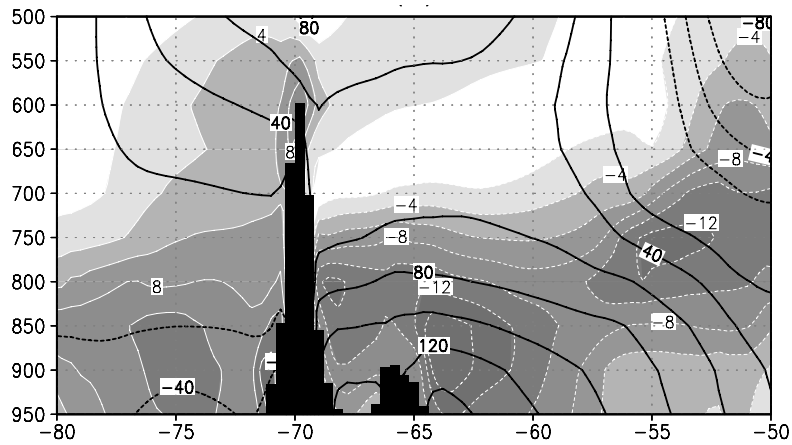


Figure 9: Vertical cross section at a) 23°S and b) 33°S of geopotential height change (contoured every 40 gpm) and temperature tendency (°C, shades) for the during the 0000 UTC April 14 to 0000 UTC April 17 (a) and 00000 UTC April 16 to 00000 UTC April 17 (b) periods. Model topographic profile is included.

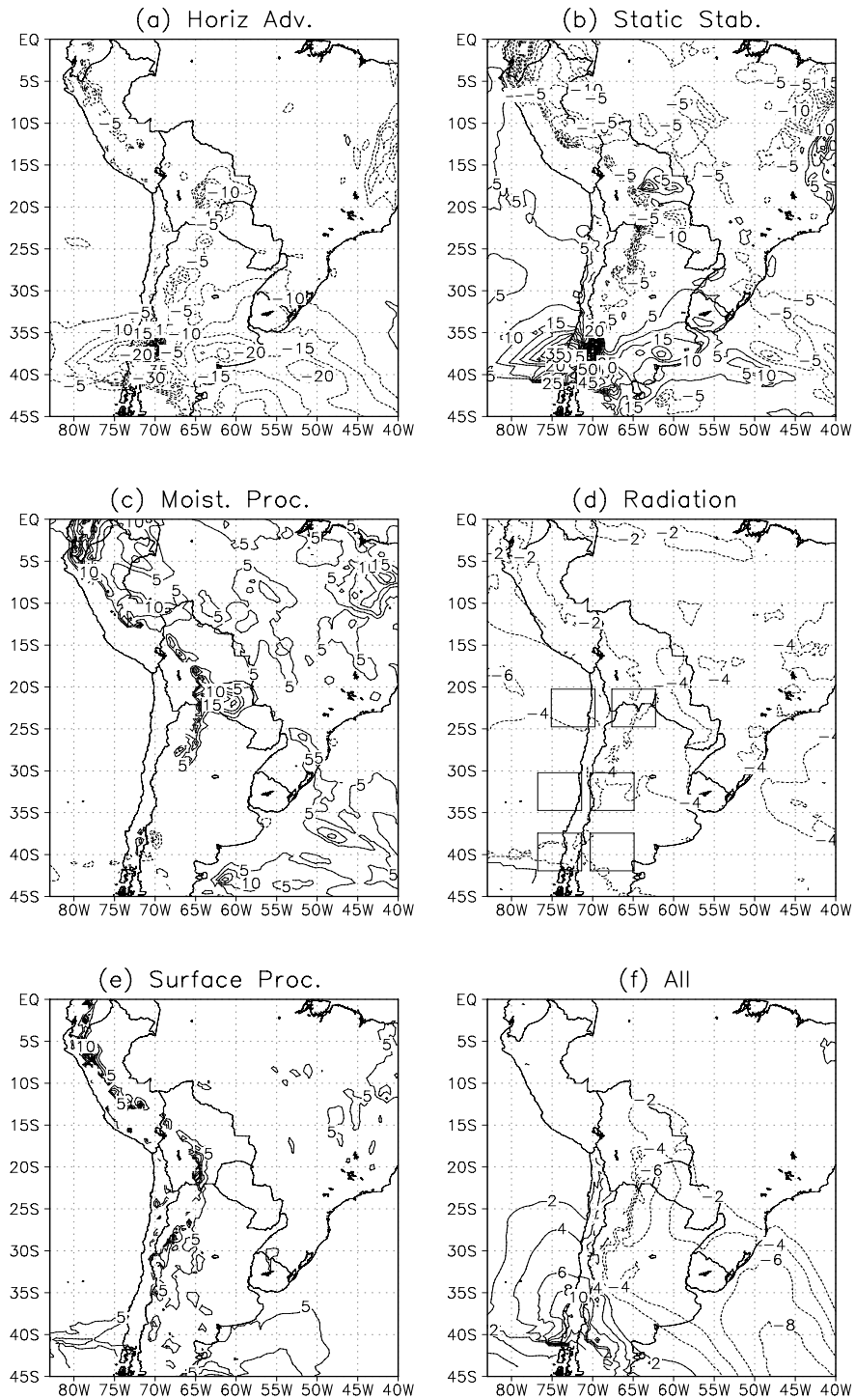


Figure 10: Temperature tendency ($^{\circ}\text{C}$) averaged between surface and 700 hPa levels associated with each of the terms of the thermodynamic equation in η coordinates (Eta/CPTEC simulation) during the active period (from 0000 UTC April 14 through 0000 UTC April 17). Boxes indicated in panel d) were used to perform the temporal evolution showed in Figure 11.

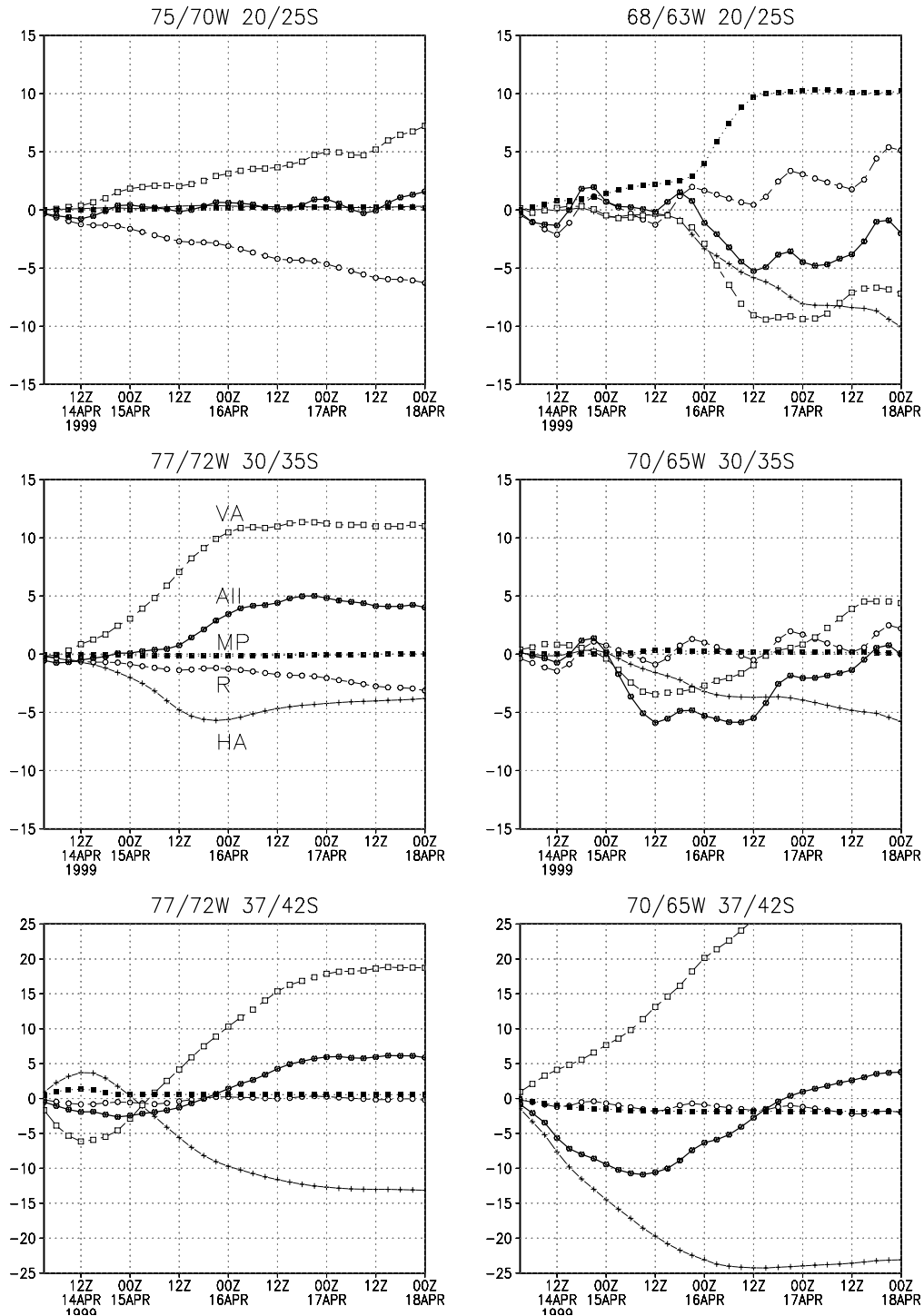


Figure 11: Temporal evolution of the temperature tendency ($^{\circ}\text{C}$) averaged between surface and 700 hPa levels associated with each of the terms of the thermodynamic equation in η coordinates (Eta/CPTEC simulation) averaged over the indicated boxes (illustrated in panel d) of Figure 10).

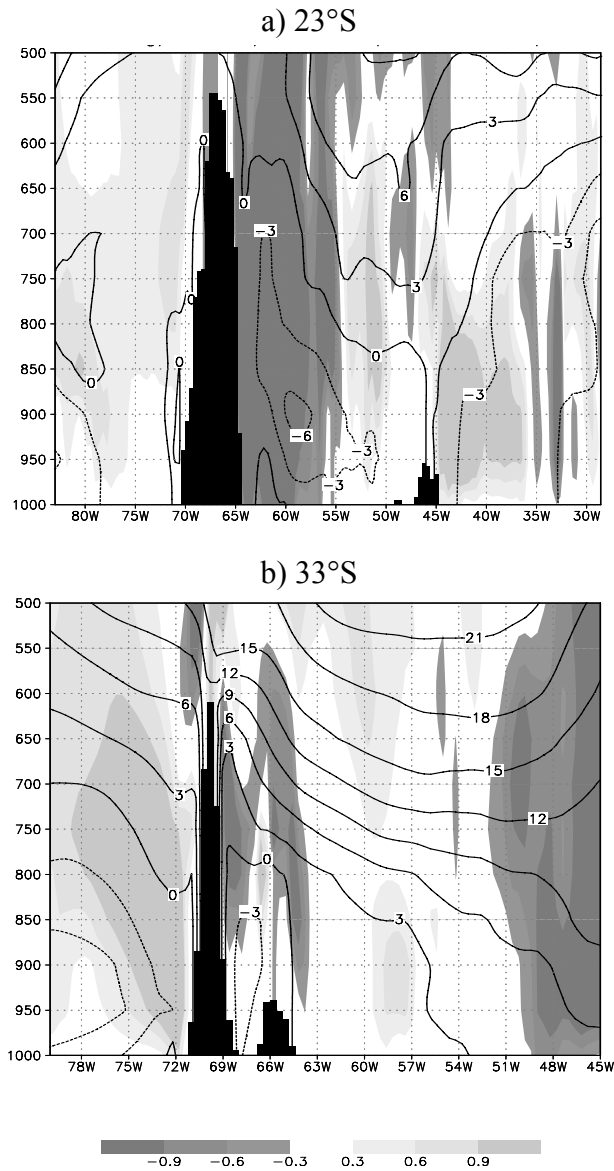


Figure 12: Vertical cross section at a) 23°S and b) 33°S of the vertical omega (hPa/s, shaded) and zonal wind (contours, m/s) averaged between a) 0000 UTC April 14 and 0000 UTC April 17 and b) 0000 16 UTC April 16 and 0000 UTC April 17 from Eta/CPTEC simulations. Model topographic profile is included.

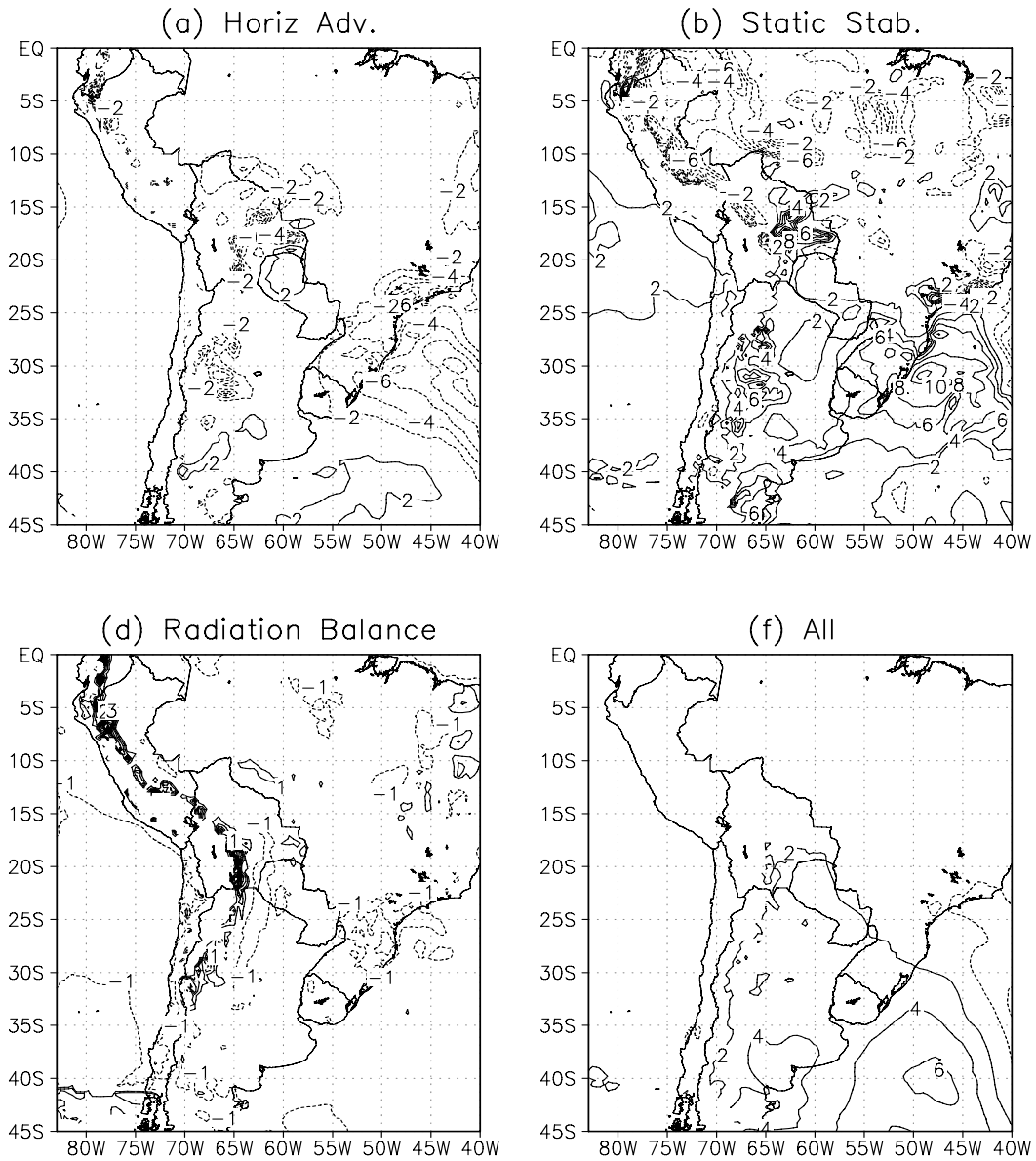


Figure 13: As Fig. 10 but for the decaying period (from 0000 UTC April 17 through 0000 UTC April 18). Panels correspond to the partial contribution of (a) horizontal advection, (b) static stability, (c) Radiation + surface processes, and (d) the sum of all the partial contributions (including those derived from moisture processes).

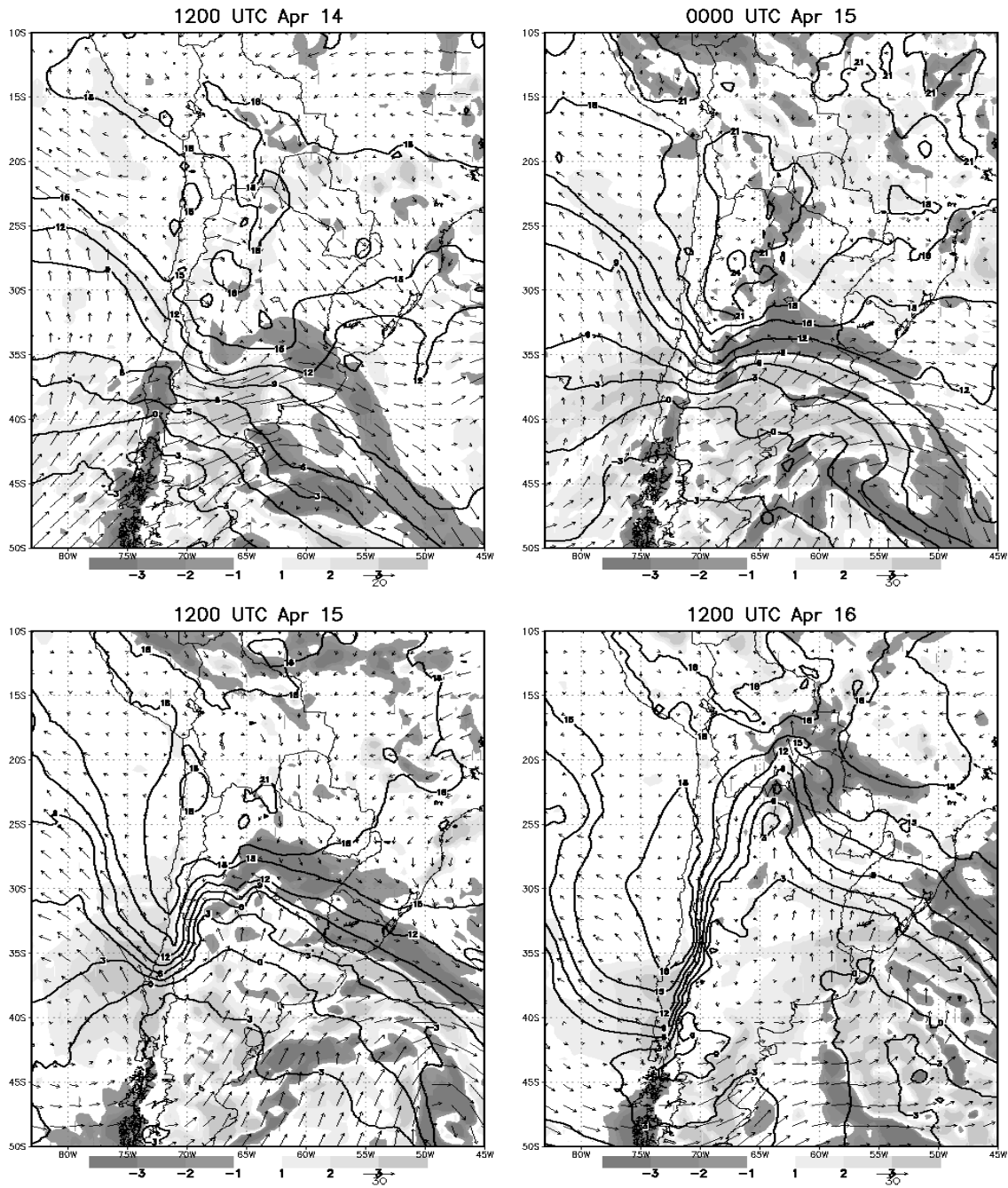


Figure 14: Temperature contours (contoured every 3°C), wind vectors (m/s) and omega vertical velocity (hPa/s) at the 850 hPa level, corresponding to 1200 UTC April 14 (upper left panel), 0000 UTC April 15 (upper right panel), 1200 UTC April 15 (lower left panel) and 1200 UTC April 16 (lower right panel).